The Astrophysical Journal, 999:183 (9pp), 2026 March 10 https://doi.org/10.3847/1538-4357/ae4101

A Black Hole Envelope Interpretation for Cosmological Demographics of Little Red Dots

Hiroya Umeda[1,2], Kohei Inayoshi[3], Yuichi Harikane[1], and Kohta Murase[4,5]
[1] Institute for Cosmic Ray Research, The University of Tokyo, 5-1-5 Kashiwanoha, Kashiwa, Chiba 277-8582, Japan; ume@icrr.u-tokyo.ac.jp
[2] Department of Physics, Graduate School of Science, The University of Tokyo, 7-3-1 Hongo, Bunkyo, Tokyo 113-0033, Japan
[3] Kavli Institute for Astronomy and Astrophysics, Peking University, Beijing 100871, People's Republic of China
[4] Department of Physics, Department of Astronomy & Astrophysics, Center for Multimessenger Astrophysics, Institute for Gravitation and the Cosmos, The Pennsylvania State University, University Park, PA 16802, USA
[5] Center for Gravitational Physics and Quantum Information, Yukawa Institute for Theoretical Physics, Kyoto University, Kyoto, 606-8502, Japan
Received 2025 December 3; revised 2026 January 25; accepted 2026 February 1; published 2026 March 3

Abstract

Little Red Dots (LRDs) newly discovered with JWST are active galactic nuclei (AGNs) that may represent black hole (BH) growth at the earliest cosmic epochs. These sources show puzzling features unlike typical AGNs, including red optical continua, weak hot-dust emission, and a lack of detectable X-rays. Previously, LRDs have often been interpreted as dust-reddened AGNs, leading to severe inconsistencies with the luminosity and BH mass densities inferred for previously known AGNs over $0 < z < 5$. The BH envelope (BHE) model has been proposed to explain these characteristics, in which an accreting BH is enshrouded by a dense, optically thick gaseous envelope. In this article, we reanalyze the spectral energy distributions of ∼400 photometric LRDs in the COSMOS-Web survey using the BHE model and reassess their implications for cosmological BH evolution. We find that the optical–near-IR spectra of LRDs are well reproduced by blackbody emission with an effective temperature of 4000–6000 K. Within the BHE framework, the inferred bolometric luminosities decrease by $\gtrsim$1–2 orders of magnitude compared to assumptions for dust-reddened AGNs. As a result, the revised luminosity function, BH accretion density, and BH mass function become consistent with those of AGNs at $z < 5$. The stellar masses of LRD hosts are estimated by attributing the UV excesses to star formation. Although the resulting $M_{\rm BH}/M_\star$ ratio remains higher than the local empirical value, the excess is modest. Overall, the BHE model not only resolves the spectral features of LRDs but also brings their statistical properties into agreement with the broader cosmological BH population.

Unified Astronomy Thesaurus concepts: Supermassive black holes (1663); Galaxy formation (595); Active galactic nuclei (16)

1. Introduction

JWST has uncovered a population of compact, red nuclei with broad emission features, known as Little Red Dots (LRDs; e.g., Y. Harikane et al. 2023; D. D. Kocevski et al. 2023; J. E. Greene et al. 2024; J. Matthee et al. 2024; H. B. Akins et al. 2025). Their rest-frame UV–optical spectra show a distinctive V-shaped continuum with an inflection point near the Balmer limit wavelength and a smooth rise toward longer wavelengths (J. E. Greene et al. 2024; D. J. Setton et al. 2024; B. Wang et al. 2024; D. D. Kocevski et al. 2025; I. Labbe et al. 2025). Their spectral energetics, compact morphologies, and broad lines indicate active black hole (BH) accretion at high redshifts (J. Matthee et al. 2024; R. E. Hviding et al. 2025), though their intrinsic luminosities and masses remain uncertain due to the poorly constrained spectral origin. While dust-reddened quasars can reproduce their red optical colors, they struggle to account for the weakness of near-to-mid infrared emission constrained by JWST/MIRI (P. G. Pérez-González et al. 2024; C. C. Williams et al. 2024; H. B. Akins et al. 2025). Moreover, the absence of X-ray emission further implies Compton-thick, super-Eddington accretion flows (P. Madau & F. Haardt 2024; K. Inayoshi et al. 2025a; R. Maiolino et al. 2025), for which the bolometric corrections are largely unconstrained even for nearby active galactic nuclei (AGNs).

A growing number of observations and theoretical studies suggest that LRDs are powered by accreting BHs enshrouded by a dense, optically thick envelope (e.g., A. de Graaff et al. 2025b; K. Inayoshi & R. Maiolino 2025; K. Inayoshi et al. 2025b; D. Kido et al. 2026; X. Lin et al. 2026a; R. P. Naidu et al. 2025). This envelope forms a photosphere that thermalizes a large fraction of the accretion power and produces a blackbody-like continuum with an effective temperature of ∼5000 K (e.g., C. Hayashi 1961). The presence of prominent Balmer absorption and break features reinforces this interpretation because hydrogen-rich photospheres at such temperatures naturally imprint these features (H. Liu et al. 2025). Theoretical models for super-Eddington flows and direct-collapse seed formation predict radiation-pressure-supported envelopes and outflows that can trap high-energy photons and reprocess the emission to optical wavelengths (M. C. Begelman & J. Dexter 2026; D. Kido et al. 2026; see also M. C. Begelman et al. 2006; T. Hosokawa et al. 2013).

Motivated by these recent developments in the context of LRDs, we revisit the LRD population with a BH envelope (BHE) model. We fit the optical bumps as photospheric emission and we quantify the statistical properties of the envelopes and the central BHs. Our analysis aims to place LRDs within a physically motivated growth pathway for early accreting BHs and to clarify how their demographics connect to super-Eddington accretion at high redshift.

Table 1
Prior Distributions for Fitting Parameters

z	$T_{\rm ph}$ ($\times 10^3$ K)	$\beta_{\rm UV}$	A_1 (nJy)	A_2 (nJy)	A_V (mag)
(1)	(2)	(3)	(4)	(5)	(6)
$U(0, 10)$	$N_{\rm t}(5, 1, -4, 4)$	$N(-2.5, 0.5)$	$U(0, [f+\sigma]_{\rm F444W})$	$\ln N(\ln A_1, \ln 2)$	$U(0, 3)$

Note. Column (1): systemic redshift. Column (2): temperature of blackbody radiation from the black hole envelope. Column (3): slope index for the power-law UV component. Column (4): amplitude of blackbody radiation at the Balmer break. Here, $[f+\sigma]_{\rm F444W}$ represents the 1σ upper error values for the observed F444W flux. Column (5): amplitude of the power-law UV component at the Balmer break. Column (6): visual extinction. $N(\mu, \sigma)$ is a normal distribution with mean μ and variance σ^2. $N_{\rm t}(\mu, \sigma, n_l, n_u)$ is a truncated normal distribution with mean μ and variance σ^2, with truncation below (above) $n_l(n_u) \times \sigma$. $U(a, b)$ is a uniform distribution between a and b. $\ln N(\mu, \sigma)$ is a log-normal distribution with mean μ and variance σ^2.

Throughout this article, we assume a flat Lambda cold dark matter cosmology consistent with the constraints from Planck (Planck Collaboration et al. 2020): $h = 0.6766$, $\Omega_{\rm m} = 0.3103$, $\Omega_\Lambda = 0.6897$, and $\Omega_{\rm b}h^2 = 0.02234$. All magnitudes are in the AB system (J. B. Oke & J. E. Gunn 1983).

2. Data and Spectral Energy Distribution Fitting

2.1. Little Red Dot Sample

In this work, we use the LRD sample presented by H. B. Akins et al. (2025), which was selected from the 0.54 deg^2 COSMOS-Web survey (GO-1727; PIs: J. Kartaltepe and C. Casey; C. M. Casey et al. 2023).[6] The selection requires a red optical color with $m_{277} - m_{444} > 1.5$, and a compact morphology in the F444W-band image. G. Barro et al. (2024) found that almost all the objects selected by this criterion are compact and appear blue at 1–2 μm. The compactness is quantified by the flux ratio measured with two aperture sizes, i.e., $0.5 < C_{444} < 0.7$, where $C_{444} = f_{444}(d = 0\farcs2)/f_{444}(d = 0\farcs5)$. This criterion selects the objects with small effective radii (i.e., $r_e \lesssim 100$–300 pc). The full LRD sample consists of 434 objects.

To improve the inference of spectral energy distributions (SEDs) at the rest-frame optical wavelengths, we additionally select objects with MIRI-band photometry to ensure multiple photometry data to constrain the shape of the optical spectrum. This fiducial LRD sample with MIRI data coverage consists of 148 objects. While we conduct the SED fitting for the full LRD sample, we only use the fiducial sample to measure the bolometric luminosity function.

2.2. Black Hole Envelope Model Fitting

H. B. Akins et al. (2025) performed SED fitting on the LRD sample to estimate their photometric redshifts and bolometric luminosities. They adopted quasar template spectra with dust attenuation, and found that the LRDs are located at photometric redshifts of $z \sim 5$–9. However, the nondetection of the rest-frame near-IR (NIR) in their multiwavelength stacking analysis of the LRDs suggests a lack of dust reemission after attenuation. Moreover, the stacking analysis of LRDs suggests nondetection of X-rays, contradicting the observational characteristics of ordinary AGNs with super-Eddington accretion. To reconcile the puzzling features of LRDs, D. Kido et al. (2026) propose the BHE model. In the BHE model, intense outflows from the central BH are confined within a massive envelope. The energy from the central engine is trapped and convected within the envelope, eventually escaping from its photosphere by blackbody radiation, similar to stars evolving along the Hayashi track. Because the photospheric radiation in the BHE model is expected to be thermal emission with an effective temperature of $\sim$4000–7000 K, its Wien tail naturally reproduces the optical V-shaped continuum while simultaneously explaining the nondetection of rest-frame NIR emission by JWST/MIRI (K. Inayoshi et al. 2025c). Motivated by the convenience of the model, we fit the SED of the LRD sample with the BHE model to estimate the photometric redshift and bolometric luminosity of the objects.

For the BHE model, we approximate the optical spectrum of LRDs by blackbody radiation with a corresponding photospheric temperature $T_{\rm ph}$. We add the break feature to the blackbody radiation at the Balmer break wavelength $\lambda_{\rm Balmer}$ (i.e., 3646 Å) to account for the Balmer absorption within the BHE. We also allow moderate dust attenuation of the blackbody radiation by changing the visual extinction value (A_V). We assume the dust attenuation law of D. Calzetti et al. (2000). The optical part of the BHE model spectrum is expressed as follows:

$$f_\nu \propto H(x) B_\nu(T_{\rm ph}) e^{-\tau_\nu(A_V)}, \quad (1)$$

where $x = \nu - c/\lambda_{\rm Balmer}$ and $H(x)$ is the Heaviside step function. We normalize the optical part of the spectrum (i.e., Equation (1)) to A_1 at the Balmer break in the observed frame. For the full spectrum model, we add a power-law spectrum with the slope $\beta_{\rm UV}$ to Equation (1) to account for the UV component of the LRD spectrum. We also normalize the power-law component to A_2 at the Balmer break in the observed frame. In addition, we add a break at the rest-frame 1216 Å to account for the Lyman break. We fit the spectra of the LRD sample with the SED model described above. We use the Markov Chain Monte Carlo (MCMC) module `PyMC` (PyMC-Devs 2025) to perform the SED fitting for the flexible sampling. We set conventional prior distributions for each parameter as listed in Table 1. We briefly explain key details of the physically and observationally motivated reasoning behind our prior selections. We vary $T_{\rm ph}$ around 3000–7000 K to match the typical photospheric temperature of the BHE model described by D. Kido et al. (2026). We also model A_1 and A_2 with mutual dependences, where A_2 is tied to A_1 to ensure a continuous transition across $\lambda_{\rm Balmer}$ and to reproduce the observed V-shaped spectral feature (e.g., A. de Graaff et al. 2025b; R. P. Naidu et al. 2025). We also limit the A_1 value to be smaller than the 1σ upper error of the observed F444W flux because the selection of H. B. Akins et al. (2025) requires an

[6] https://hollisakins.com/projects/1_project/

elevated rest-frame optical (i.e., blackbody) component compared to the UV component. We also vary A_V around 0–3 to account for relatively weak dust continuum emission in the infrared (e.g., H. B. Akins et al. 2025). For the photometric data, we use the all available photometry provided by H. B. Akins et al. (2025). For the nondetection band, we utilize the 3σ upper limit and create the likelihood function following the method of M. Sawicki (2012). To estimate the detection limit in each band, we fitted a linear relation between the signal-to-noise ratio and the flux uncertainty provided in the original catalog of H. B. Akins et al. (2025). The catalog contains photometry from the Hubble Space Telescope (HST)/Advanced Camera for Surveys (ACS), JWST/ NIRCam, and JWST/MIRI imaging. From the COSMOS-Web data, we use HST/ACS F814W and JWST/NIRCam F115W, F150W, F277W, F444W, and JWST/MIRI F770W filters. For sources covered by the PRIMER survey (GO-1837; PI. James Dunlop; J. S. Dunlop et al. 2021), we additionally include photometry from the following filters: HST/ACS F666W and F814W, JWST/NIRCam F090W, F115W, F150W, F200W, F277W, F356W, F410M, F444W, and JWST/MIRI F770W and F1800W. To reduce the impact of outliers caused by strong emission lines, we adopt a likelihood function that is robust to such deviations. Instead of the commonly used Gaussian likelihood, we employ a Student's t-likelihood, defined as

$$\phi(f_i^{\rm obs}|\boldsymbol{\theta}) = \frac{\Gamma((\nu+1)/2)}{\sqrt{\nu\pi}\,\sigma_i\Gamma(\nu/2)} \times \left(1+\frac{1}{\nu}\left(\frac{f_i^{\rm obs}-f_i^{\rm model}(\boldsymbol{\theta})}{\sigma_i}\right)^2\right)^{-(\nu+1)/2}. \quad (2)$$

We adopt the degree of freedom $\nu = 1$ for the Student's t-distribution. We also adjust the nondetection term of the cumulative likelihood function based on the Student's t-distribution:

$$\Phi(f_{i,\rm up}^{\rm obs}|\boldsymbol{\theta}) = \int_{-\infty}^{f_i^{\rm obs,up}} \phi(x|\boldsymbol{\theta})dx, \quad (3)$$

where $f_{i,\rm up}^{\rm obs}$ is the 3σ upper limit flux for the nondetection band. The total likelihood function is expressed as follows:

$$\mathcal{L}(\boldsymbol{\theta}|\boldsymbol{f}^{\rm obs}) = \prod_i^{N_{\rm det}} \phi(f_i^{\rm obs}|\boldsymbol{\theta}) \prod_j^{N_{\rm non-det}} \Phi(f_{j,up}^{\rm obs}|\boldsymbol{\theta}). \quad (4)$$

We perform MCMC sampling with 20 parallel chains and 20,000 steps per chain.

2.3. Fitting Result

In Figure 1, we present an example of the fitting for one LRD candidate (i.e., COS-145575 of H. B. Akins et al. 2025). The left panel of Figure 1 presents the corner diagram representing both the 1D and 2D marginalized posterior probability distributions. The median posterior spectrum obtained from our SED fitting is shown in the right panel. We also present the model photometry, calculated by convolving the model spectrum with the filter transmission curves. Our model and the observed photometry are consistent within 1σ error bars in all imaging bands. For comparison, we show the best-fit QSO spectrum from H. B. Akins et al. (2025). Unlike standard QSO templates, H. B. Akins et al. (2025) introduce an additional unattenuated intrinsic component to reproduce the unusually blue UV continuum together with a very red optical component. Their QSO model spectrum resembles an LRD spectrum, with enhanced optical flux due to strong emission lines and suppressed UV emission caused by dust attenuation. However, the QSO model would produce high rest-frame near-infrared flux values from the strong dust reemission, which is hard to reconcile with the nondetections in the near-infrared in the stacked spectra (H. B. Akins et al. 2025).

Table 2 summarizes the median posterior values for our sample. To further compare our inferences with previous work, we directly compare the estimates of bolometric luminosity for individual LRDs. We adopt the bolometric luminosities from H. B. Akins et al. (2025) (i.e., $\log L_{\rm bol,QSO}$), which they derived with their dusty QSO spectral model. For our BHE model, we compute the bolometric luminosity, $\log L_{\rm bol,BHE}$, by integrating the intrinsic (unattenuated) blackbody spectrum. We do not include the UV power-law component in our bolometric luminosity measurement. As shown in Figure 2, the bolometric luminosities based on BHE and dusty QSO models differ significantly. $L_{\rm bol,BHE}$ typically amounts to only $\sim$2% of $L_{\rm bol,QSO}$. H. B. Akins et al. (2025) adopt a dusty QSO SED with $A_V \sim 3$ for LRDs, so that the strongly attenuated UV emission is reprocessed into the near-infrared, thereby elevating the inferred bolometric output. In contrast, our BHE model reproduces the optical SED with more modest dust attenuation, $A_V \sim 1$, because the blackbody continuum naturally explains the observed optical bump. The resulting bolometric correction from the rest-frame 5100 Å luminosity is $\simeq$4.4 in the BHE model, slightly smaller than the canonical value of $\sim$10 commonly adopted for local blue quasars (G. T. Richards et al. 2006). The combination of the reduced dust attenuation at optical wavelengths (flux suppression factor $\sim 10^{-0.4(3-1)} \simeq 0.16$) and the smaller bolometric correction for the dust-attenuation–corrected spectrum (factor $\sim[4.4\times10^{-0.4}]/10 \simeq 0.18$) jointly accounts for the low normalization, yielding $L_{\rm bol,BHE} \simeq 0.02 L_{\rm bol,QSO}$. We checked the robustness of the bolometric luminosity measurements by refitting the SED by sampling $\log(T_{\rm BB}/{\rm K})$ in the uniform prior range of 3–4 and confirmed that the bolometric luminosity measurements are mostly consistent with our fiducial results within 0.3 dex and do not affect our overall discussions. Because the BHE framework replaces the dusty QSO interpretation in earlier work and yields substantially lower bolometric luminosities for LRDs, population-level quantities such as the luminosity function and the BH accretion density should be revised accordingly.

The right panel of Figure 2 shows the bolometric luminosity and photospheric temperature of LRDs in the Hertzsprung–Russell (H-R) diagram. Most LRDs lie within a narrow range of $T_{\rm eff} \simeq 4500$–6000 K, consistent with the features of the stellar atmosphere expected in the BHE model as well as the independent temperature measurements based on the spectroscopic data (A. de Graaff et al. 2025a). This characteristic temperature range physically arises from the photospheric conditions governed by H^- opacity, as discussed for cool, inflated gaseous envelopes surrounding rapidly growing BHs (e.g., M. C. Begelman & J. Dexter 2026; K. Inayoshi et al. 2025c; D. Kido et al. 2026). By analogy with red giant stars on

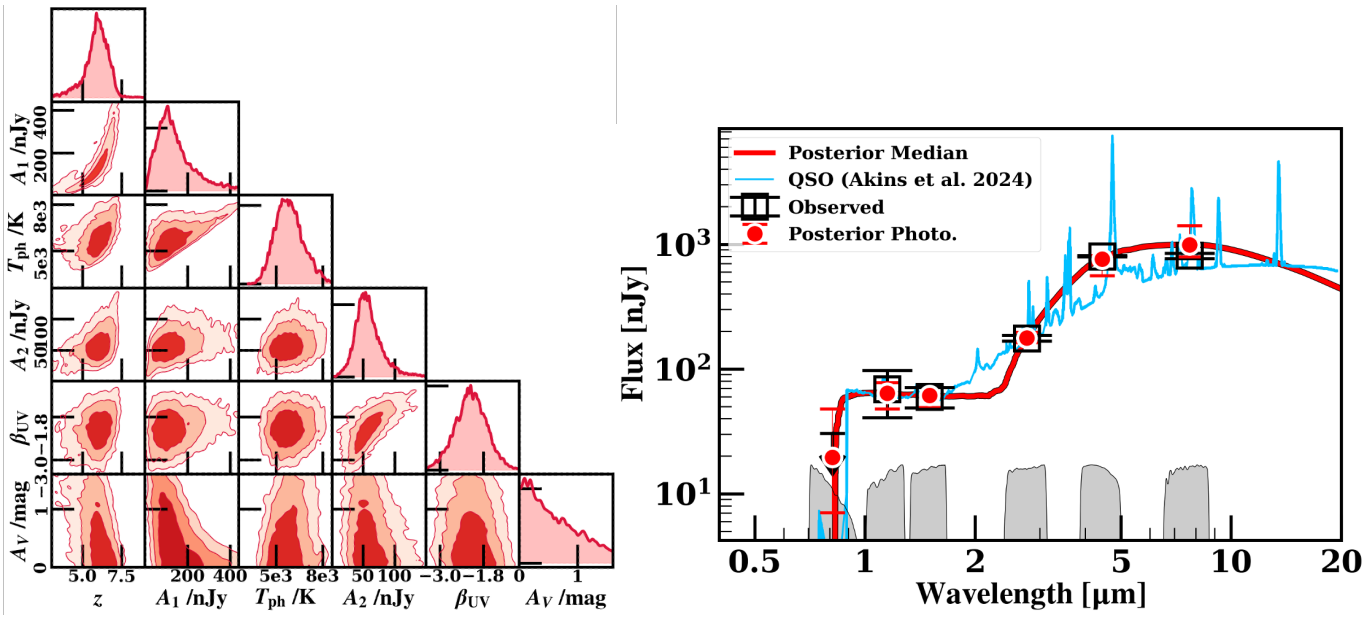

Figure 1. Left: example posterior distribution from the SED fitting. The top panels in each column represent the 1D marginalized probability distribution function (PDF) for the corresponding parameters, while the remaining panels display the 2D marginalized PDFs for each pair of parameters. Right: posterior PDF of the BHE-based SED fitting for one LRD from H. B. Akins et al. (2025; COS-145575). Black data points with error bars show the observed photometric fluxes. The red solid line indicate a SED realization drawn from the posterior PDF, and the red points show the corresponding model photometric fluxes and uncertainties. The median and 68th percentile parameter constraints are as follows: $z = 6.00^{+0.64}_{-0.77}$, $A_1/\mathrm{nJy} = 124^{+101}_{-58}$, $T_{\rm ph}/\mathrm{K} = 5670^{+820}_{-690}$, $A_2/\mathrm{nJy} = 56.3^{+22.6}_{-16.5}$, $\beta_{\rm UV} = -2.14^{+0.43}_{-0.44}$, and $A_V/\mathrm{mag} = 0.55^{+0.72}_{-0.40}$. The shaded curves at the bottom of the panel represent the transmission curves of the filters used in the fitting.

Table 2
Summary of Posterior Inferences from BHE Modeling of the LRD Sample

Quantity	Value
$T_{\rm ph}$ (K)	5420^{+240}_{-200}
A_V (mag)	$0.93^{+0.31}_{-0.27}$
$L_{\rm bol}/\lambda L_{\lambda,5100}$	$4.41^{+2.12}_{-1.37}$

Note. Values are medians with 16th and 84th percentile uncertainties for the LRD sample.

the H-R diagram, we also indicate the region obtained by extrapolating the Hayashi track (C. Hayashi 1961) toward higher luminosities from the locus of red supergiant stars in the Milky Way. We note that while the photospheric conditions in the BHE framework have been discussed analytically (M. C. Begelman & J. Dexter 2026; D. Kido et al. 2026), many of the detailed structural and thermal properties remain poorly constrained and will require further investigation.

The photospheric radius, i.e., the outermost layer of the envelope structure, is estimated from the luminosity and surface temperature through the Stefan–Boltzmann law as

$$R_{\rm ph} \simeq 0.01\ \mathrm{pc}\left(\frac{L_{\rm bol}}{10^{11}\,L_\odot}\right)^{1/2}\left(\frac{T_{\rm eff}}{5000\ \mathrm{K}}\right)^{-2}. \quad (5)$$

Most LRDs have photospheric radii of $R_{\rm ph} \simeq 4 \times 10^{-3}$ pc. A useful comparison is with the size of the broad-line region (BLR). M. C. Bentz et al. (2013) derived the empirical BLR size–luminosity relation from reverberation mapping of local AGNs with $\lambda L_{\lambda,5100} = 10^{42}$–$10^{46}\,\mathrm{erg\,s^{-1}}$. Applying this relation to the typical $\lambda L_{\lambda,5100}$ value, the BLR size of LRDs is $R_{\rm BLR} \simeq 8 \times 10^{-3}(L_{\rm bol}/10^{11}\,L_\odot)^{1/2}$ pc, which is systematically larger than the photospheric radii of the envelope. This size comparison suggests that the BLR would likely reside just outside the inflated envelope. In this configuration, BLR clouds may be powered either by ionizing radiation escaping through polar funnels of the thick envelope structure (see Figure 14 of X. Lin et al. 2026a) or by ionizing radiation produced by young stellar populations surrounding the BHE structure (see Figure 1 of K. Inayoshi et al. 2025b). These possibilities can be tested through future, long-term monitoring of BLR variability.

3. Revisiting Statistical Properties of LRDs

3.1. Luminosity Function

Based on the inferred SED parameters, we calculate the bolometric luminosity function for LRDs. We divide the sample into redshift bins of $5 < z < 7$ and $7 < z < 9$ to calculate the AGN luminosity function at $z \sim 6$ and 8, respectively. We also consider the completeness correction based on H. B. Akins et al. (2025). We calculate the comoving volume for each redshift bin based on the survey area of COSMOS-Web covered by MIRI, which is 0.19 deg^2. We estimate the completeness as a function of $L_{\rm bol}$ by anchoring our measurements to the luminosity function of H. B. Akins et al. (2025). First, for each $L_{\rm bol}$ bin of H. B. Akins et al. (2025), we compute the completeness as the ratio between their luminosity function and the raw number density of detected LRDs in that bin. We then map this completeness function to our $L_{\rm bol}$ bins using the nearly linear relation between the bolometric luminosities inferred by H. B. Akins et al. (2025) and by our BHE modeling (Figure 2). We adopt the mapped values as the completeness in our analysis. We summarize the LRD number densities, binned by bolometric luminosities reestimated under the BHE model, in Table 3.

We show our LRD luminosity function for $z \sim 6$ and 8 in Figure 3. For comparison, we also plot the QSO luminosity function from the literature based on the X-ray observations

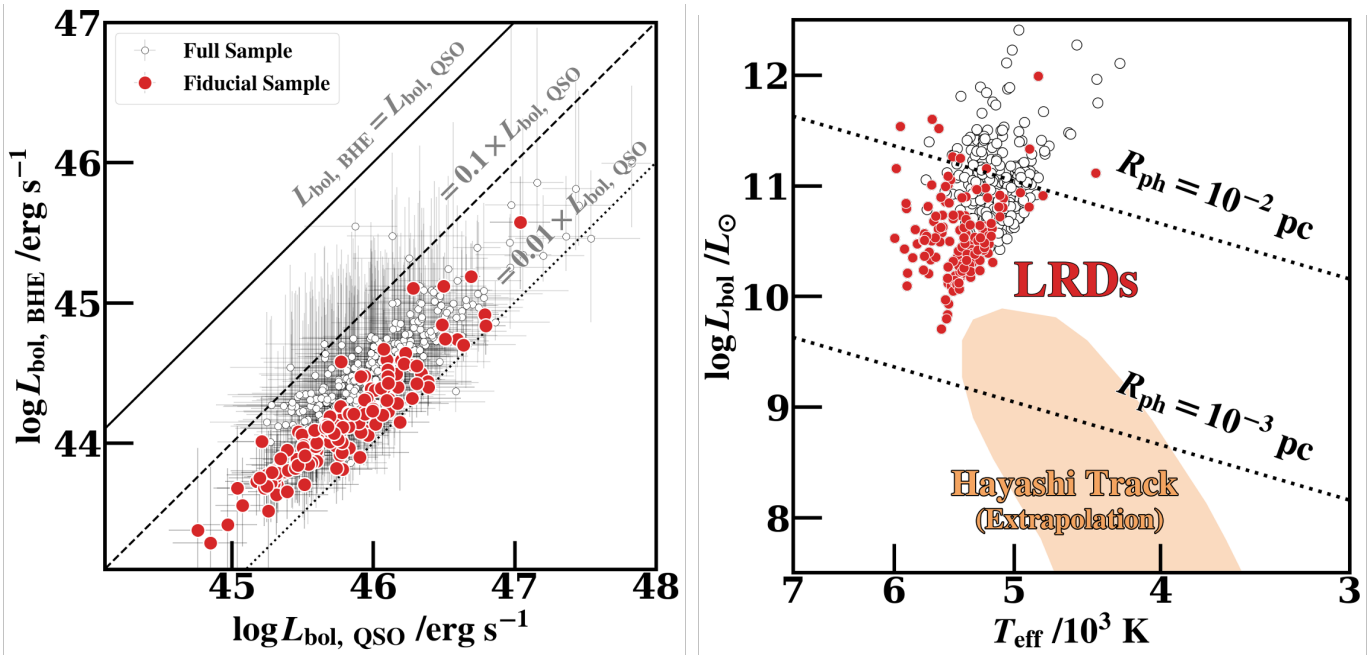

Figure 2. Left: comparison of the bolometric luminosities between the BHE model ($L_{\rm bol,BHE}$) and the dust-reddened AGN model ($L_{\rm bol,QSO}$). The solid, dashed, and dotted lined represent $L_{\rm bol,BHE}/L_{\rm bol,QSO} = 1.0$, 0.1, and 0.01, respectively. Right: Hertzsprung–Russell diagram for the fiducial LRD sample (red circles) and full sample (open circles), showing effective temperatures and luminosities under the assumption of blackbody spectra. Dotted lines indicate the loci of constant photospheric radius of $R_{\rm ph} = 10^{-3}$ and 10^{-2} pc. The narrow temperature range over $T_{\rm eff} \simeq 4500$–6000 K is consistent with the tip of the Hayashi track extrapolated from from the locus of red supergiant stars in the Milky Way (shaded region).

Table 3
Bolometric-luminosity-binned Number Densities of LRDs Inferred under the BHE Model at $z \sim 6$ and $z \sim 8$

$\log(L_{\rm bol}/{\rm erg\ s^{-1}})$	$\phi_{\rm LRD}(z\sim6)$ (cMpc$^{-3}\,\Delta\log L_{\rm bol}^{-1}$)	$\Delta\phi_{\rm LRD}(z\sim6)$ (cMpc$^{-3}\,\Delta\log L_{\rm bol}^{-1}$)	$\phi_{\rm LRD}(z\sim8)$ (cMpc$^{-3}\,\Delta\log L_{\rm bol}^{-1}$)	$\Delta\phi_{\rm LRD}(z\sim8)$ (cMpc$^{-3}\,\Delta\log L_{\rm bol}^{-1}$)
43.5	1.18×10^{-4}	3.06×10^{-5}	...	...
44.0	6.38×10^{-5}	7.79×10^{-6}	4.92×10^{-5}	1.74×10^{-5}
44.5	2.78×10^{-5}	5.45×10^{-6}	1.18×10^{-5}	5.26×10^{-6}
45.0	1.11×10^{-5}	5.56×10^{-6}	3.94×10^{-6}	3.94×10^{-6}
45.5	4.07×10^{-6}	4.07×10^{-6}	...	...

Note. $\phi_{\rm LRD}$ denotes the comoving number density of Little Red Dots. Uncertainties (i.e., $\Delta\phi_{\rm LRD}$) represent Poisson errors.

(Y. Ueda et al. 2014) and the high-z QSO survey by the ground-based telescope (M. Niida et al. 2020; Y. Matsuoka et al. 2023). For the rest-frame UV and X-ray-selected sources, we apply calibrations from F. Duras et al. (2020) to convert the observed UV/X-ray luminosities to the bolometric luminosities. Unlike the claims that the LRD number density is excessive (e.g., J. C. J. D'Silva et al. 2025), our estimates of number density lie around the extrapolated faint end of the bright QSO luminosity function. The mitigation of apparent LRD overabundance mainly results from the reduction in the inferred bolometric luminosity by adopting the BHE model. We also show the bolometric luminosity function derived by J. E. Greene et al. (2026). They estimated a bolometric correction factor of $\simeq$5 for the 5100 Å luminosity by interpolating and extrapolating the fluxes from UV to infrared wavelengths of LRD spectra with high signal-to-noise ratio and integrating the resulting SED. They recalculated the LRD bolometric luminosity function from J. E. Greene et al. (2024) based on the new correction factor. The bolometric correction factor of 4.4 and the luminosity function we derive with the BHE framework are in good agreement with the results of J. E. Greene et al. (2026).

3.2. Black Hole Mass Function

We infer the black hole mass function (BHMF) using the bolometric luminosity. The bolometric luminosity of the BH physically relates to its mass via the following relation:

$$M_{\rm BH} = \frac{\sigma_T}{4\pi c G m_p} \times \frac{L_{\rm bol}}{\lambda_{\rm Edd}} \simeq 0.81 \times 10^5\, M_\odot\, \lambda_{\rm Edd}^{-1} \left(\frac{L_{\rm bol}}{10^{43}\ {\rm erg\ s^{-1}}}\right). \quad (6)$$

Here, $\lambda_{\rm Edd}$ denotes the Eddington ratio. We adopt a fiducial value of $\lambda_{\rm Edd} = 0.5$ to reflect the near-Eddington accretion state expected in the BHE model. We also consider $\lambda_{\rm Edd} = 0.1$ and 1, and incorporate the systematic variation into the uncertainties of the BH mass measurement. For reference, we plot the BHMF derived from the bolometric luminosity function of H. B. Akins et al. (2025) in the dust-reddened AGN hypothesis with $\lambda_{\rm Edd} = 0.5$. We additionally present the BHMF at $z \simeq 6$ (cyan) and $z \simeq 8$ (red) in Figure 4.

We further compare our results to the BHMF of AGNs at $z \sim 5$ inferred from single-epoch virial mass estimates (W. He et al. 2024; J. Matthee et al. 2024; A. J. Taylor et al. 2025). The BHMF derived under the BHE model lies below the $z \sim 5$

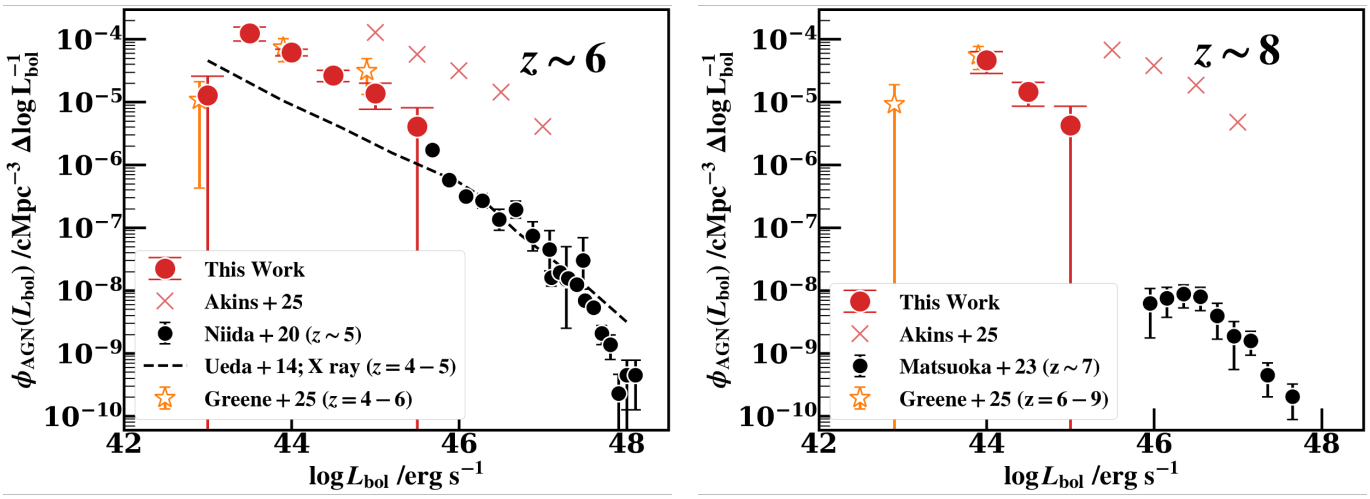

Figure 3. Left: the bolometric luminosity function of the AGNs at $z \sim 6$. The number density of LRDs is shown by the red circles. We adopt a bolometric luminosity of LRDs based on the BHE model. We also present the bolometric luminosity function of QSOs based on the Subaru surveys by M. Niida et al. (2020), shown with black circles. The dashed line represents the luminosity function inferred from the X-ray observations from Y. Ueda et al. (2014). The red crosses represent the luminosity function from H. B. Akins et al. (2025) derived assuming the QSO model. We also show the bolometric luminosity function from J. E. Greene et al. (2026) by the open yellow stars. Right: the bolometric luminosity function of the AGNs at $z \sim 8$. The number density of the LRDs is shown with red circles. We adopt the bolometric luminosity of LRDs based on the BHE model. We also present the bolometric luminosity function of QSOs based on the Subaru surveys by Y. Matsuoka et al. (2023), shown with black circles. Other legends represents the same thing as they do in the left panel.

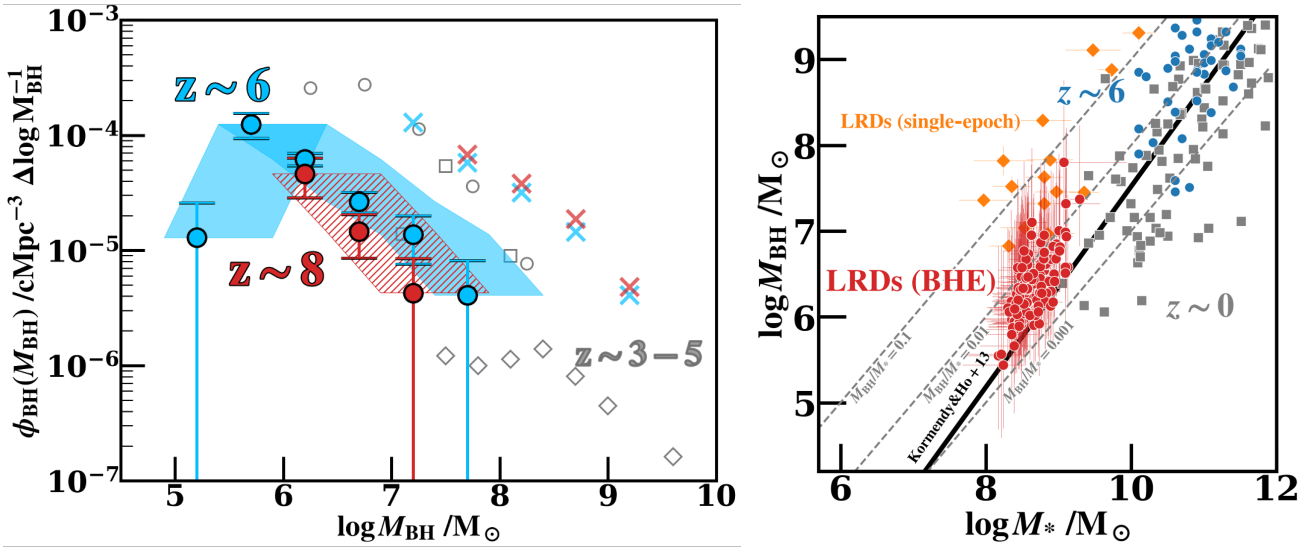

Figure 4. Left: black hole mass functions of LRDs at $z \sim 6$ (blue) and $z \sim 8$ (red). Black hole masses are estimated from the bolometric luminosity in the BHE model, assuming $\lambda_{\rm Edd} = 0.5$ (filled circles). For each redshift, the shaded region denotes the BHMF range obtained with $\lambda_{\rm Edd} = 0.1$–1. Cross symbols show the BHMF inferred under the dust-reddened AGN hypothesis (H. B. Akins et al. 2025) with $\lambda_{\rm Edd} = 0.5$. For the comparison, BHMF constraints for AGNs at $z = 3$–5 derived from single-epoch virial mass estimates are overlaid with open symbols (circle: A. J. Taylor et al. 2025, square: J. Matthee et al. 2024, diamond: W. He et al. 2024). Right: relation between host stellar mass and black hole mass for LRDs in the BHE framework (red circles) including uncertainties from the assumed $\lambda_{\rm Edd}$ values. Measurements of the $M_{\rm BH}$–$M_\star$ relation at $z = 0$ (gray square and black diagonal line: J. Kormendy & L. C. Ho 2013) and $z \sim 6$ (blue circle: T. Izumi et al. 2021) are shown for comparison. The LRD population tends to be overmassive ($M_{\rm BH}/M_\star \simeq 0.005$) relative to the local relation, although the offset is moderate. Black hole masses inferred from the Hα-based single-epoch method (D. D. Kocevski et al. 2025) are also plotted (orange diamonds). Dashed lines indicate $M_{\rm BH}/M_\star = 10^{-3}$, 10^{-2}, and 10^{-1}.

virial-based BHMF. We find no strong redshift evolution between $z \sim 6$ and 8. However, we observe an order-of-magnitude drop from $z \sim 5$ to $z \simeq 6$ at fixed mass, which may partly arise from the differences in estimating the BH mass.

3.3. Stellar Mass to Black Hole Mass Relation

Based on our BH mass measurements, we revisit the stellar mass and BH mass relation based on our SED fitting results using the BHE model. According to the BHE model of K. Inayoshi et al. (2025b), the UV continuum radiation blueward of the Balmer break is attributed to stars. Therefore, we can derive the stellar mass from the UV luminosity assuming the scaling relation between UV luminosity and star formation rate (SFR) and that the host galaxy lies in the SFR–$M_\star$ main sequence. For the conversion factor between UV luminosity and SFR, we assume the scaling law as follows:

$$\mathrm{SFR}/M_\odot\ \mathrm{yr}^{-1} = 1.15 \times 10^{-28}\, L_{\rm UV}\ /\mathrm{erg\ s^{-1}\ Hz^{-1}}. \quad (7)$$

Here, we adopt a constant SFR and a Salpeter initial mass function (IMF; 0.1–100 $M_\odot$), assuming stellar ages >300 Myr

and a characteristic metallicity of $\sim 0.5\,Z_{\odot}$, for which the results depend only weakly on metallicity (P. Madau & M. Dickinson 2014). For the star-forming main sequence, we adopt the empirical relation of P. Popesso et al. (2023). They used a sample of galaxies at $0 < z < 6$ spanning stellar masses of 10^{8}–$10^{12}\,M_{\odot}$ to derive the following empirical calibration between stellar mass and SFR (i.e., Equation (10) of P. Popesso et al. 2023):

$$\begin{aligned}\log(\mathrm{SFR}/M_{\odot}\ \mathrm{yr}^{-1}) = {} & (a_1 t(z) + b_1)\log(M_{\star}/M_{\odot}) \\ & + b_2 \log^2(M_{\star}/M_{\odot}) \\ & + (b_0 + a_0) t(z). \end{aligned} \quad (8)$$

Here, $t(z)$ corresponds to the age of the Universe at z in Gyr. We use the best-fit value for the coefficients (i.e., a_0, a_1, b_0, b_1, and b_2) listed in Table 2 of P. Popesso et al. (2023) with a correction to match to the Salpeter IMF. In Figure 4, we present our estimate of stellar and BH mass for the LRD sample. We also present the local $M_{\star}$–$M_{\rm BH}$ relation from J. Kormendy & L. C. Ho (2013) and the measurements of $z \sim 6$ quasars (T. Izumi et al. 2021). We find that the majority of $M_{\rm BH}/M_{\star}$ ratios of LRDs measured with the BHE model lie on or slightly above the local relation and $z \sim 6$ quasars. We compare our results with the $M_{\rm BH}/M_{\star}$ measurements of LRDs from D. D. Kocevski et al. (2025), which are derived using an empirical relation between $M_{\rm BH}$ and the broad emission lines. We see that $M_{\rm BH}/M_{\star}$ measurements based on the BHE model are about 1–2 orders of magnitude lower than those based on the broad-line relations at the fixed stellar mass. This offset aligns with the deviation between the BHMF derived using the BHE model and that based on the empirical relation. We note, however, that the current sample of LRDs with detected broad lines may be biased toward overmassive BHs, because only the most luminous broad-line systems are detectable at the survey depth. We therefore conservatively suggest that the BHE model offers a plausible way to alleviate the apparent tension between the stellar mass and BH mass relations for LRDs. Further tests of this scenario will require larger and deeper spectroscopic samples of LRDs.

3.4. Black Hole Accretion Density

Next, we calculate the BH accretion density for the LRDs using the inferred bolometric luminosity from the BHE model. The mass accretion rate of the black hole $\dot{M}_{\rm BH}$ can be expressed in terms of bolometric luminosity in the following manner:

$$\dot{M}_{\rm BH} = \frac{1 - \epsilon_{\rm rad}}{\epsilon_{\rm rad}} \times \frac{L_{\rm bol}}{c^2}, \quad (9)$$

where $\epsilon_{\rm rad}$ represents the radiative efficiency of the accreting BH. We adopt a fiducial value of $\epsilon_{\rm rad} = 0.1$ as commonly assumed in the literature (e.g., A. Soltan 1982; Q. Yu & S. Tremaine 2002; Y. Ueda et al. 2014). The radiative efficiency may be reduced when the BH accretes at rates exceeding the Eddington limit as expected in the BHE model. Radiation-hydrodynamic simulations show that even when gas is supplied at highly super-Eddington rates on large scales, convection within the envelope suppresses the net inflow toward the BH, so that the BH is actually fed at only mildly super-Eddington rates of $\dot{M}_{\rm BH} = \mathcal{O}(1-10) \times \dot{M}_{\rm Edd}$. Under these conditions, the radiative efficiency decreases by a factor of $\simeq 2$ relative to the canonical value (e.g., Y.-F. Jiang et al. 2019; K. Inayoshi et al. 2020). Despite the uncertainty in $\epsilon_{\rm rad}$, we adopt $\epsilon_{\rm rad} = 0.1$ as our baseline value to maintain consistency with the literature and to allow direct comparison, while noting that moderate deviations from this choice would not alter our main conclusion.

We then estimate the black hole accretion rate density (BHAD) traced by the observed LRDs by integrating their luminosity function down to the COSMOS-Web detection limit and converting the bolometric luminosity density into mass accretion density using Equation (9). We present our BHAD measurements in Figure 5 with the BHAD constrained from literature using mid-IR (I. Delvecchio et al. 2014) and X-ray observations (J. Aird et al. 2015; T. T. Ananna et al. 2019; E. Pouliasis et al. 2024). We find that the BHAD of LRDs at $z \sim 6$–8 lies on the extrapolated high-redshift tail of the BHAD constraints from the lower-redshift observations. For the reference, we also calculate the BHAD contributed by a $z > 10$ LRD candidate (T. S. Tanaka et al. 2025). We adopt the estimated number density and the bolometric luminosity (i.e., $L_{\rm bol} \sim 3 \times 10^{44}\,\mathrm{erg\,s^{-1}}$) inferred by T. S. Tanaka et al. (2025) with BHE model. Reduction of the inferred luminosity using the BHE model naturally reconciles the overshooting BHAD values inferred from the ordinary QSO template models. Moreover, the smooth connection between the BHAD inferred at $z < 5$ from X-rays and at $z > 5$ from LRDs suggests that the LRD phase may have played a dominant role in the BH mass accumulation at the epoch of cosmic reionization. The gradual transition from the LRD-dominated to the X-ray-emitting, normal AGN population through super-Eddington accretion around $z \sim 5$ may possibly mark the emergence of ordinary quasars after the LRD phase.

3.5. Evolution of Black Hole Mass Density

According to Soltan's argument, the cumulative mass accreted onto BHs should match the total BH mass density in the local Universe. In Figure 5, we present present the BH mass density of LRDs ($\rho_{\rm BH}$) inferred from their observed abundance, along with the increase in their mass density ($\Delta\rho_{\rm BH}$) obtained by integrating the BHAD over the time interval of each redshift bin (i.e., $\Delta\rho_{\rm BH} \simeq \mathrm{BHAD} \times \Delta t$). We find that $\Delta\rho_{\rm BH}$ contributed by LRDs is smaller by a factor of several than the total BH mass growth at the corresponding redshifts. The comparison between the observed $\rho_{\rm BH}$ of LRDs at $z \sim 6$ and the cumulative $\Delta\rho_{\rm BH}$ produced during the LRD phase from $z = 10$ to $z = 6$ suggests that the LRD phase has a duty cycle of about 20%. This inferred value is consistent with the duty cycle estimated from clustering analyses (i.e., $\sim$40%; J. Arita et al. 2025), although other clustering-based studies indicate even lower values (e.g., $\sim$1%; X. Lin et al. 2026b).

To check the consistency between the high- and low-redshift BH populations, we present the observationally constrained $\rho_{\rm BH}$ in the local Universe from F. Shankar et al. (2009) together with $\Delta\rho_{\rm BH}$ calculated from the AGN BHAD at $0 < z < 5$ assuming $\epsilon_{\rm rad} = 0.1$ (Y. Ueda et al. 2014). The cumulative mass accretion from the ordinary AGN population at $0 < z < 5$ smoothly connects $\rho_{\rm BH}$ for $z = 0$ and $\Delta\rho_{\rm BH}$ for $z > 6$ from LRDs, implying that mass accretion with a radiative efficiency of $\epsilon_{\rm rad} \simeq 0.1$ is consistent with Soltan's argument over $0 \lesssim z \lesssim 10$ (see also F. Zou et al. 2024).

In Figure 5, we also plot measurements of the redshift evolution of star formation rate density from Y. Harikane et al.

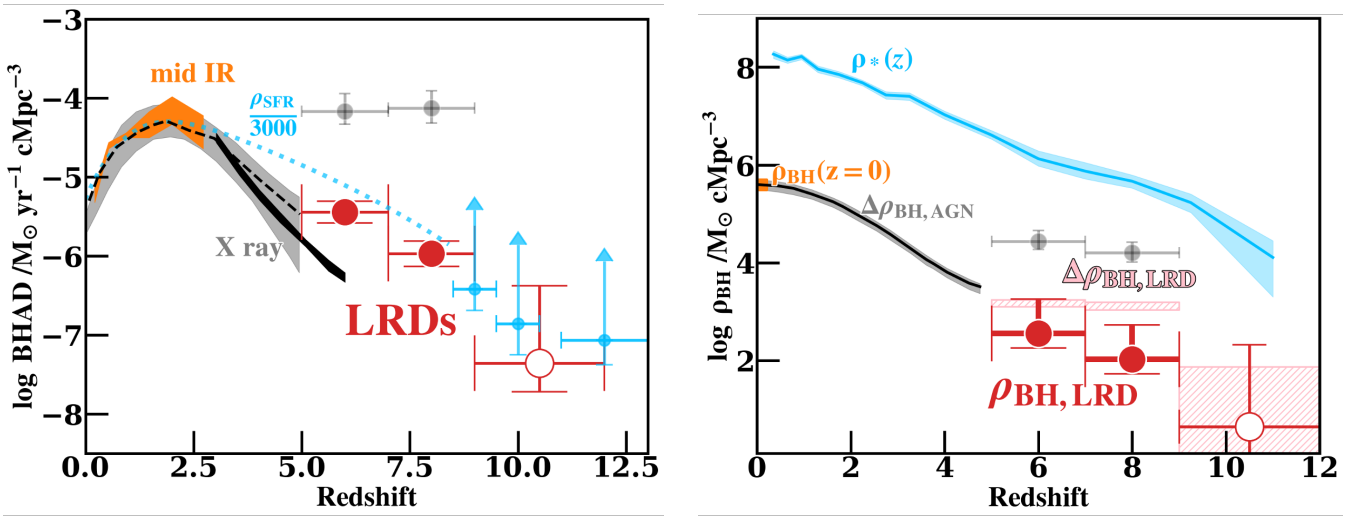

Figure 5. Left: black hole accretion density of LRDs as a function of redshift (red circles). BHADs are estimated from the bolometric luminosity function based on the BHE model, assuming $\epsilon_{rad} = 0.1$. Measurements based on the $z \sim 6$–8 LRD sample of H. B. Akins et al. (2025) (filled) and $z \sim 10$ LRDs (open) from T. S. Tanaka et al. (2025) are shown together with original BHAD measurements from H. B. Akins et al. (2025) with the QSO model (gray circles). For the comparison we present BHAD constraints from observations in the mid-IR (orange: I. Delvecchio et al. 2014) and X-rays (gray region: J. Aird et al. 2015, black region: E. Pouliasis et al. 2024, black dashed line: T. T. Ananna et al. 2019). We also plot the redshift evolution of star formation rate density ρ_{SFR} as blue symbols (dotted line: Y. Harikane et al. 2022, circles: Y. Harikane et al. 2025). We scale ρ_{SFR} by a factor of 1/3000 to match the BHAD at $z < 3$. Right: the black hole mass density by redshifts. The red circles represent ρ_{BH} derived from integrating the BHMF of LRDs at $z = 6$ and 8. The open circle represent ρ_{BH} estimated using a $z > 10$ LRD candidate reported by T. S. Tanaka et al. (2025). The error bars include the systematic offset arising from adopting $\lambda_{Edd} = 0.1$ versus $\lambda_{Edd} = 1$. The pink shades represents the 1σ upper and lower limit ranges $\Delta\rho_{BH}$ calculated from integrating the BHAD of LRDs over time (Δt) corresponding to the redshift binning width. The gray circles represent $\Delta\rho_{BH}$ estimated based on BHAD assuming the QSO model (H. B. Akins et al. 2025). The orange region represents ρ_{BH} at $z = 0$ measured by F. Shankar et al. (2009). The black solid line represents $\Delta\rho_{BH}$ estimated from the BHAD of $0 < z < 5$ ordinary AGNs with $\epsilon_{rad} = 0.1$ (Y. Ueda et al. 2014). For the comparison, we plot recent measurements of stellar mass density from M. Shuntov et al. (2025) as a blue line.

(2022, 2025) along with BHAD evolution, and measurements of stellar mass density from M. Shuntov et al. (2025) along with the evolution of BH mass density. With a normalization of SFR density by a factor of 3000, the redshift evolution of BHAD and SFR density coincide with one another. Moreover, we find that the stellar and BH mass densities evolve in parallel with redshift up to $z \sim 10$. The parallel evolution between stellar and BH mass densities at $0 < z < 10$ could possibly indicate the coevolution of BH and host galaxies from the early stage of BH formation. Such coevolution may be driven by linked mass assembly, in which efficient cold-stream gas inflows feed the central regions of dark matter halos (e.g., A. Dekel & Y. Birnboim 2006), while subsequent supernova feedback from the young nuclear stellar cluster disrupts the LRD phase (K. Inayoshi et al. 2025b). Together, these processes could possibly provide a natural pathway for the concurrent buildup of BH and stellar mass, ultimately giving rise to the tight BH–stellar mass correlations observed in the local Universe.

4. Conclusion

In this article, we have reanalyzed the COSMOS-Web LRD sample using the BHE model, which describes super-Eddington accretion surrounded by an optically thick envelope. The BHE model reproduces the characteristic optical V-shaped continuum through photospheric emission at $T_{ph} \sim 4000$–6000 K and naturally explains the lack of far-infrared detections without invoking heavy dust obscuration. The inferred bolometric luminosities are typically 1–2 dex lower than those derived from quasar templates, bringing the number densities of LRDs into agreement with the faint-end extrapolation of known AGN luminosity functions. The resulting BHMF and accretion rate density smoothly connect to those of ordinary AGNs at $z \lesssim 5$, suggesting that LRDs represent a short-lived, efficient growth phase in the early buildup of supermassive BHs. Expanded MIRI coverage from programs such as COSMOS-3D (GO-5893; PI. Koki Kakiichi; K. Kakiichi et al. 2024) will improve constraints on the rest-frame optical-to-NIR spectral properties of LRDs. Future spectroscopy (e.g., EMBER program; GO-7076; PI: Hollis Akins) and variability monitoring will be crucial to confirm the physical nature and duty cycle of this LRD phase.

Acknowledgments

We thank Hollis Akins and COSMOS-Web teams led by Jeyhan Kartaltepe and Caitlin Casey for the public data release of COSMOS-Web and the LRD catalog. We thank Masami Ouchi, Kunihito Ioka, Tatsuya Matsumoto, Hiroto Yanagisawa, Mitsuru Kokubo, and Takumi Tanaka for useful comments and discussions. This work is based on observations with the NASA/ESA/CSA James Webb Space Telescope at the Space Telescope Science Institute, which is operated by the Association of Universities for Research in Astronomy, Inc., under NASA contract NAS 5-03127 for JWST. H.U. acknowledges support from the World Premier International Research Center Initiative (WPI Initiative), MEXT, Japan, and KAKENHI (20H00180) through Japan Society for the Promotion of Science, the joint research program of the Institute for Cosmic Ray Research (ICRR), University of Tokyo, and FoPM WINGS Program in the University of Tokyo. K.I. acknowledges support from the National Natural Science Foundation of China (12573015, W2532003), the Beijing Natural Science Foundation (IS25003), and the China Manned Space Program (CMS-CSST-2025-A09). Y.H. acknowledges support from the JSPS Grant-in-Aid for Scientific Research (24H00245) and the JSPS International Leading Research (22K21349). The work of K.M.

was supported by KAKENHI No. 20H05852 and the Institute for Gravitation and the Cosmos of the Pennsylvania State University. We thank the Yukawa Institute for Theoretical Physics at Kyoto University. Discussions during the YITP workshop YITP-W-25-08 on Exploring Extreme Transients were useful to complete this work.

ORCID iDs

Hiroya Umeda https://orcid.org/0009-0008-0167-5129
Kohei Inayoshi https://orcid.org/0000-0001-9840-4959
Yuichi Harikane https://orcid.org/0000-0002-6047-430X
Kohta Murase https://orcid.org/0000-0002-5358-5642

References

Aird, J., Coil, A. L., Georgakakis, A., et al. 2015, MNRAS, 451, 1892
Akins, H. B., Casey, C. M., Lambrides, E., et al. 2025, ApJ, 991, 37
Ananna, T. T., Treister, E., Urry, C. M., et al. 2019, ApJ, 871, 240
Arita, J., Kashikawa, N., Onoue, M., et al. 2025, MNRAS, 536, 3677
Barro, G., Pérez-González, P. G., Kocevski, D. D., et al. 2024, ApJ, 963, 128
Begelman, M. C., & Dexter, J. 2026, ApJ, 996, 48
Begelman, M. C., Volonteri, M., & Rees, M. J. 2006, MNRAS, 370, 289
Bentz, M. C., Denney, K. D., Grier, C. J., et al. 2013, ApJ, 767, 149
Calzetti, D., Armus, L., Bohlin, R. C., et al. 2000, ApJ, 533, 682
Casey, C. M., Kartaltepe, J. S., Drakos, N. E., et al. 2023, ApJ, 954, 31
de Graaff, A., Hviding, R. E., Naidu, R. P., et al. 2025a, arXiv:2511.21820
de Graaff, A., Rix, H.-W., Naidu, R. P., et al. 2025b, A&A, 701, A168
Dekel, A., & Birnboim, Y. 2006, MNRAS, 368, 2
Delvecchio, I., Gruppioni, C., Pozzi, F., et al. 2014, MNRAS, 439, 2736
D'Silva, J. C. J., Driver, S. P., Lagos, C. D. P., et al. 2025, ApJ, 990, 44
Dunlop, J. S., Abraham, R. G., Ashby, M. L. N., et al. 2021, JWST Proposal 1837, 2021jwst.prop.D
Duras, F., Bongiorno, A., Ricci, F., et al. 2020, A&A, 636, A73
Greene, J. E., Labbe, I., Goulding, A. D., et al. 2024, ApJ, 964, 39
Greene, J. E., Setton, D. J., Furtak, L. J., et al. 2026, ApJ, 996, 129
Harikane, Y., Inoue, A. K., Ellis, R. S., et al. 2025, ApJ, 980, 138
Harikane, Y., Ono, Y., Ouchi, M., et al. 2022, ApJS, 259, 20
Harikane, Y., Zhang, Y., Nakajima, K., et al. 2023, ApJ, 959, 39
Hayashi, C. 1961, PASJ, 13, 450
He, W., Akiyama, M., Enoki, M., et al. 2024, ApJ, 962, 152
Hosokawa, T., Yorke, H. W., Inayoshi, K., Omukai, K., & Yoshida, N. 2013, ApJ, 778, 178
Hviding, R. E., de Graaff, A., Miller, T. B., et al. 2025, A&A, 702, A57
Inayoshi, K., Kimura, S. S., & Noda, H. 2025a, PASJ, 77, 811
Inayoshi, K., & Maiolino, R. 2025, ApJL, 980, L27
Inayoshi, K., Murase, K., & Kashiyama, K. 2025b, arXiv:2509.19422
Inayoshi, K., Shangguan, J., Chen, X., Ho, L. C., & Haiman, Z. 2025c, arXiv:2505.05322
Inayoshi, K., Visbal, E., & Haiman, Z. 2020, ARA&A, 58, 27
Izumi, T., Matsuoka, Y., Fujimoto, S., et al. 2021, ApJ, 914, 36
Jiang, Y.-F., Stone, J. M., & Davis, S. W. 2019, ApJ, 880, 67
Kakiichi, K., Egami, E., Fan, X., et al. 2024, JWST Proposal 5893,
Kido, D., Ioka, K., Hotokezaka, K., Inayoshi, K., & Irwin, C. M. 2026, MNRAS, 544, 3407
Kocevski, D. D., Finkelstein, S. L., Barro, G., et al. 2025, ApJ, 986, 126
Kocevski, D. D., Onoue, M., Inayoshi, K., et al. 2023, ApJL, 954, L4
Kormendy, J., & Ho, L. C. 2013, ARA&A, 51, 511
Labbe, I., Greene, J. E., Bezanson, R., et al. 2025, ApJ, 978, 92
Lin, X., Fan, X., Cai, Z., et al. 2026a, ApJ, 997, 364
Lin, X., Fan, X., Sun, F., et al. 2026b, ApJ, 997, 61
Liu, H., Jiang, Y.-F., Quataert, E., Greene, J. E., & Ma, Y. 2025, ApJ, 994, 113
Madau, P., & Dickinson, M. 2014, ARA&A, 52, 415
Madau, P., & Haardt, F. 2024, ApJL, 976, L24
Maiolino, R., Risaliti, G., Signorini, M., et al. 2025, MNRAS, 538, 1921
Matsuoka, Y., Onoue, M., Iwasawa, K., et al. 2023, ApJL, 949, L42
Matthee, J., Naidu, R. P., Brammer, G., et al. 2024, ApJ, 963, 129
Naidu, R. P., Matthee, J., Katz, H., et al. 2025, arXiv:2503.16596
Niida, M., Nagao, T., Ikeda, H., et al. 2020, ApJ, 904, 89
Oke, J. B., & Gunn, J. E. 1983, ApJ, 266, 713
Pérez-González, P. G., Barro, G., Rieke, G. H., et al. 2024, ApJ, 968, 4
Planck Collaboration, Aghanim, N., Akrami, Y., et al. 2020, A&A, 641, A6
Popesso, P., Concas, A., Cresci, G., et al. 2023, MNRAS, 519, 1526
Pouliasis, E., Ruiz, A., Georgantopoulos, I., et al. 2024, A&A, 685, A97
PyMC-Devs 2025, PyMC, v5.25.1, Zenodo, doi:10.5281/zenodo.4603970
Richards, G. T., Lacy, M., Storrie-Lombardi, L. J., et al. 2006, ApJS, 166, 470
Sawicki, M. 2012, PASP, 124, 1208
Setton, D. J., Greene, J. E., de Graaff, A., et al. 2024, ApJ, 995, 118
Shankar, F., Weinberg, D. H., & Miralda-Escudé, J. 2009, ApJ, 690, 20
Shuntov, M., Ilbert, O., & Toft, S. 2025, A&A, 695, A20
Soltan, A. 1982, MNRAS, 200, 115
Tanaka, T. S., Akins, H. B., Harikane, Y., et al. 2025, ApJ, 995, 21
Taylor, A. J., Finkelstein, S. L., Kocevski, D. D., et al. 2025, ApJ, 986, 165
Ueda, Y., Akiyama, M., Hasinger, G., Miyaji, T., & Watson, M. G. 2014, ApJ, 786, 104
Wang, B., Leja, J., de Graaff, A., et al. 2024, ApJL, 969, L13
Williams, C. C., Alberts, S., Ji, Z., et al. 2024, ApJ, 968, 34
Yu, Q., & Tremaine, S. 2002, MNRAS, 335, 965
Zou, F., Brandt, W. N., Gallo, E., et al. 2024, ApJ, 976, 6